Supporting Information

Bastiaansen et al.

SI 1. Dimensional extended-Klausmeier

The dimensional extended-Klausmeier model is given by Eq. (SI 1.1). The model used throughout the paper, Eq. (1), can be obtained from the dimensional version by the right set of scaling. Following (1, Appendix A), the required scaling is given in Eq. (SI 1.2) for the variables and in Eq. (SI 1.3) for the parameters of the model.

$$\begin{cases} \frac{\partial W}{\partial T} &= E\frac{\partial^2 W}{\partial X^2} + \frac{\partial (VW)}{\partial X} + A - LW - RWN^2 \\ \frac{\partial N}{\partial T} &= D\frac{\partial^2 N}{\partial X^2} + RJWN^2 - MN \end{cases} \quad \text{[SI 1.1]}$$

$$w = \frac{\sqrt{R}J}{\sqrt{L}}W \quad n = \frac{\sqrt{R}}{\sqrt{L}}N \quad x = \frac{\sqrt{L}}{\sqrt{D}}X \quad t = LT \quad \text{[SI 1.2]}$$

$$a = \frac{\sqrt{R}J}{L\sqrt{L}}A \quad m = \frac{1}{L}M \quad v = \frac{1}{\sqrt{LD}}V \quad e = \frac{E}{D} \quad \text{[SI 1.3]}$$

In these equations, water is supplied to the system at a rate $+A$, modeling uniform rainfall. Because of evaporation, water is lost at a rate $-LW$; water is also lost through uptake by plants, at rate $-RWN^2$. The parameter J models the increase of biomass per unit of water consumed, which results in the reproduction of plants at rate $+RJWN^2$. Plant mortality is modeled as $-MN$. The parameter V is the speed at which water flows downhill; this is proportional to the slope gradient. Finally, E is the diffusion coefficient of water; D is the diffusion coefficient of vegetation, modeling the dispersal of biomass. See also (2).

SI 2. Description of study sites

For this study, two sites in Somalia were selected that exhibit mostly banded vegetation. The Haud site is a $35km$ by $28km$ study area ($8°0'14''$ to $8°15'11''$N; $47°11'54''$ to $47°31'4''$E) at 650-750m elevation in the Haud pastoral region – see also Figure S2. Here, banded vegetation dominates the landscape with some minor occurrences of gapped vegetation on flat ground on the summits of rolling hills. Bands display a broad range of wavelengths (from $60m$ to $200m$). Ground slope ranges from 0 to 1%. Mean annual precipitation, ranging from $210mm$ to $270mm$, is distributed in two rainy seasons around spring (April–May) and fall (September–November) separated by two dry seasons. Rainfall data was extracted from Climate Hazards Group InfraRed Precipitation with Stations (3). Estimates were provided by (4).

In the north-eastern corner of this area near Kalabaydh city, the soils of the bands and inter-bands are very similar (5). Moreover, the large perennial tussock grass *Andropogon kelleri* dominates the core of the band along with some scattered small trees and bushes (5). Characteristically, plants are sparsely distributed on the downslope side of the bands. Along this edge and below it, in the bare inter-band, dead trees of all of the species found within the bands were present. Along the bands' upslope side, some initial colonization by two perennial grass species, tussock-forming *Chrysopogon aucheri var. quinqueplumis* and *stoloniferous Dactyloctenium scindicum*,

was observed (5). Although the lifespan of perennial grasses is highly variable, ranging from less than a year to multiple decades (6), the average lifespan of perennial grasses in arid and semi-arid environments is typically 1-7 years (6–8). Upon inspection of satellite imageries taken 39 years apart, an upslope migration speed of $0.3m\ yr^{-1}$ was observed (9).

The Sool site is an approximately $77km$ by $29km$ study site, located $190km$ to the NE of the Haud site ($9°18'49''$ to $9°34'34''$N; $48°8'15''$ to $48°43'15''$E); it is located in the Sool-Plateau pastoral area, which has more arid conditions ($100mm$-$140mm$) and higher elevations ($900m$-$1000m$) – see also Figure S2. Here, the ground slope ranges from 0 to 1%, and ground is either bare or covered with banded vegetation which sometimes displays a dashed physiognomy. To the authors knowledge, there is no published record of the composition of these vegetated bands and associated soils. Remote sensing analysis of vegetation dynamic in this area over the last decades have shown a continuous upslope migration of the bands as well as a change in band width. However, no change in wavelength has been observed (9, 10).

SI 3. Data sets

A. Topographical data. For both sites, topographical data was retrieved from the ALOS World 3D 30m (AW3D30, v. 2.1) digital raster elevation model. This model describes the height above sea level (in m, rounded to the nearest integer), at a ground resolution of approximately 30m at the equator. The elevation data was preprocessed for the removal of artifacts by applying a global soft-thresholding on its dual tree complex wavelet transform. Specifically, we set a threshold of 0.9 on the first five dual-tree complex wavelet transform levels. From the preprocessed data, we calculated the slope gradient (in %) and slope aspect (in degrees). We first extracted square DEM windows of 33 by 33 cells (i.e. approximately $990m \times 990m$), centered on the image windows. We then applied a least squares fitting procedure of an unconstrained quadratic surface on the unweighted elevation values. From the first derivatives of this fitted surface, evaluated at the focal cell, we could then calculate slope gradient and aspect analytically, following (1). Complex topographic features were discarded from subsequent analysis by ignoring windows (see below) with quadratic fit RMSE above 1m or a total curvature (as defined by (11)) above 10^{-10} radians per m^2.

B. Biomass measurements. Recently, a map has been made with data on (above-ground) biomass of African savannahs and woodlands at a resolution of 25m (12), which provides the biomass data of the patterns studied in this article. This map is built from 2010 L-band PALSAR mosaic produced by JAXA following a method adapted from (13), while the perturbing sources that affect the SAR data have been minimized: the environmental effects (soil and vegetation moisture) were reduced by stratifying the African continent into wet/dry season areas, and the speckle noise inherent to SAR data acquisitions was decreased by applying a multi-image filter developed by (14) that preserves the spatial resolution of the images. Then, the

sensitivity of the radar backscatter to AGB was analyzed to develop a direct model relating the PALSAR backscatter to AGB, calibrated with the help of in-situ and ancillary data. The in-situ data were composed of 144 selected field plots, located in 8 countries (Cameroon, Burkina Faso, Malawi, Mali, Ghana, Mozambique, Botswana and South Africa), with plot size larger than $0.25ha$ and a mean plot size of $0.89ha$.

C. Optical data. Three multispectral WorldView-2 images, acquired on December 25th 2011, January 21st 2012 and July 21st 2012, were mosaicked and used as reference orthoimage for the Haud site. For the diachronic study, a panchromatic Ikonos "Geo" imagery, with a $1m$ nominal ground resolution, was used as the reference layer. It was acquired on January 7th 2006. Orthorectification was performed using a rational polynomial coefficient (RPC) camera model block adjustment without ground control points (15).

A mosaic of six WorldView-2 images, acquired between February 3rd 2011 and September 12th 2013, was used for the Sool sites. For the diachronic study, a panchromatic SPOT4 image preprocessed to level 2A, with a $10m$ nominal ground resolution, was use as reference layer (©Cnes 2004 – Spot Image distribution). It was acquired on February 18th 2004.

Two $7\mu m$ digitized panchromatic declassified Corona spy satellite image, national intelligence reconnaissance system, available from the USGS, were acquired on February 28th 1967 (KH-4A, mission 1039, AFT camera) and December 12th 1967 (KH-4B, mission 1102, FWD camera), respectively for the Haud and the Sool. The images were co-registered with the orthorectified reference imagery. Co-registration was performed using a third-order polynomial adjustment using landmarks such as geological features, crossroads, isolated trees, or large termite nests. We obtained an RMS adjustment error below the KH-4A ground resolution, which is $3m$ for this area. The resolution of the imagery was then lowered through pixel averaging to match the coarsest image pair.

The analysis of pattern wavelength was performed over the full area of the study sites. However, for the diachronic study, a subset of each of the sites covered by the historic and reference image was selected. Projection and datum for all data sets were WGS 1984, UTM Zone 38N and 39N respectively for the Haud and the Sool sites.

SI 4. Data processing

A. Spectral analysis, direction of anisotropy and wavelength.
On visible light digital images over drylands, bright pixels correspond to bare soil, intermediate gray-scale levels to closed grass cover, and darker pixels to woody vegetation. As a first approximation, gray-scale levels can thus be considered as a monotonically decreasing function of the aboveground biomass (16). This approximation allows us to analyze the spatiotemporal dynamics of biomass organization through image analysis techniques.

We used a Fourier windowing technique equivalent to short time Fourier transforms to obtain spatial maps of dominant pattern wavelength λ and orientation θ from the satellite images as previously used for banded vegetation systems (17–20). We applied a two-dimensional (2D) Fourier transform to obtain the power spectrum within square, non-overlapping moving windows. In order to maintain resolution and signal-to-noise ratio a boxcar windowing function to signal was applied.

This choice is, in this case, reasonable as only one periodic component is expected to be present in the vegetation. The technique provides information about the local wave-vector $k = k_x\hat{x} + k_y\hat{y}$. The two-dimensional (2D) fast Fourier transform $\tilde{f}(k_x, k_y)$ of the pattern of biomass $f(x, y)$ was obtained for each window $\tilde{f}(k)$ of size $L \times L$. As L increases, the spatial resolution, i.e. localization in space of frequency or orientation change, is reduced. Conversely, as L decreases, the frequency resolution is decreased, i.e. the likelihood of separating frequency components close together in Fourier space. To optimize both, L was chosen to be at least 3λ, i.e. $750m$ and $1010m$ respectively for the Haud and the Sool sites.

To separate the characteristics of the signal that are meaningful for this study, each k, of frequency $2\pi/\lambda$ (wavenumber), was decomposed into its orientation θ and its magnitude. For each window, the power spectrum $S(k) = |\tilde{f}(k)|^2$ was computed. The power spectrum measures how the variation, or power, of the pattern is distributed over the wavevectors k, of different frequencies and spatial directions. To identify the dominant k in each window, $S(k)$ was binned into annular rings of unit width (21). The resulting radial spectrum thus quantifies the contribution of successive ranges of spatial frequencies to the image variance across all orientations.

To deconvolve the natural $1/k$ scaling of the power spectrum, the total power within each annular ring, $S(k)$, was computed instead of the mean power. The location peak of this total power is used to define the most energetic wavenumber, k_1. To compensate for the discrete k-resolution in Fourier space, the location of the weighted average $k_1 := \left(\sum_k kS(k)\right) / \left(\sum_k S(k)\right)$ was computed over all rings that formed part of the peak and contained more than 70% of the peak power.

The patterns were characterized in terms of level and orientation of anisotropy (i.e. direction orthogonal to the long axis of the bands) following (19). The average pattern orientation was studied using the circular mean direction weighted by the power spectrum values, $\bar{\theta} := \frac{1}{2}\arctan2(S, C)$, where $S := \left(\sum_k 2k_{x,y} \sin\theta_{x,y}\right) / \left(\sum_k k\right)$ and $C := \left(\sum_k 2k_{x,y} \cos\theta_{x,y}\right) / \left(\sum_k k\right)$. The norm of the resultant vector, $\bar{R} := \sqrt{S^2 + C^2} / \left(\sum_k k\right)$, was used as an index of pattern anisotropy. The division by the sum of periodogram amplitudes ensures bounding between zero (perfect isotropy) and one (all variance concentrated in one direction, i.e. perfect bands). Pattern orientation features were extracted from the power spectrum, within the frequency ring characterizing periodic vegetation patterns, i.e. between 0.4 and 2.5 cycles $100m^{-1}$ for both the Haul and the Sool site, to exclude anisotropy sources resulting from large scale gradients or small scale (anthropogenic) features.

B. Pattern classification.
The vegetation cover of each window was quantified by converting the gray-scale intensity image to a binary image using the Otsu thresholding method (22). Windows with less than 15% vegetation cover were considered as bare soil and discarded. Windows with dominant patterns within the acceptable range (i.e. between 0.4 and 2.5 cycles $100m^{-1}$ for both sites) and with anisotropy index above 0.2 were considered as banded patterns.

C. Cross-spectral analysis and migration speed.
Scale specific comparisons between pairs of periodic 2D signals – in this case, images taken at different dates – can be performed

through 2D Fourier cross-spectral analysis. In principle, this means identifying the frequencies and orientations of patterns dominating in any two images as well as possible shifts among them. Correction of radiometric variability between dates is not required since Fourier coefficients are invariant to linear rescaling of gray-scale levels. A detailed mathematical development of the analysis can be found in (23). The procedure can be summarized as follows (9, 10).

To assess band migration distance for each temporal pair of image windows, a coherency spectrum and a phase spectrum were computed. The coherency spectrum expresses the correlation between the frequency components of the Fourier spectra of the pair of windows. For each spatial frequency, the coherency value is interpreted in a similar way to the classical Pearson's coefficient but in absolute values, because the sign of the correlation is expressed by the phase spectrum. For each window pair, the maximum value of coherency and its associated frequency were recorded along the direction of maximal anisotropy computed for the first acquisition date. Window pairs with a maximum coherency below 0.9 were rejected from the analysis, because this indicates that pattern characteristics (wavelength and orientation) changed between the dates. Rejected windows often corresponded to man-made perturbations or ephemeral patterns, which are not the subject of this study. The obtained frequency value therefore corresponds to a pattern of constant scale and orientations dominating at both acquisition dates. The corresponding phase-spectrum value provides the phase difference, i.e., the angular distance, between the selected frequency components at both dates in the maximal anisotropy direction. This value is defined between -180 and 180 degrees, with the sign representing the forward $(+)$ vs. backward $(-)$ displacement, with the direction of reference as the upslope direction. Angular distances were then converted into meters by multiplying the phase difference by the wavelength, which in turn were converted to an average migration speed for the time period. This conversion allows for inter-site comparisons independent of varying time intervals. An inherent limitation to this procedure is that only migration distances not exceeding half the wavelength will be correctly estimated (phase saturation). This condition was verified by visual inspection prior to image analysis.

D. Assessment of uncertainty in calculations of slope gradient and aspect from topographical data. As the digital raster elevation model contains errors, these will propagate into derived estimates of slope gradient and aspect. Ideally, one would use ground observations (e.g. using differential global navigation satellite systems) to assess the magnitude of these errors (e.g. (24)). Since such observations are not available for our study areas, we used a simulation method to evaluate the propagation of error from the elevation data to the estimates of slope gradient and aspect. Specifically, we created artificial elevation grids with a fixed (from here referred to as 'true') slope and aspect, and added to these grids (normally distributed) random errors with a similar standard deviation as observed in the AW3D30 dataset. The resulting elevation values were rounded to the nearest integers, as this is also done in the AW3D30 dataset. Then, utilizing the same procedures as described above (see section SI 3A), we derived slope gradients and aspects from these simulated grids. Comparison of this 'observed' slope and aspect and the 'true' slope and aspect of the grid yielded insight in the propagation of errors

from the elevation model to the calculated metrics. Seven fixed slope levels were considered: 0; 0.025; 0.05; 0.1; 0.2; 0.3 and 0.4%. For each level, we simulated $10,000$ replicate grids of errors that were added to the fixed slope level. For each replicate, the aspect was a randomly assigned value between 0 and 360 degrees.

Following the above procedure, we found that the distributions of errors in the calculated slope gradients and aspects were relatively small, for all slope levels considered (Figure S4). Because the estimated slope is bounded between zero and positive infinity, a small positive bias was observed for slopes less than 0.1%. For slopes of 0.025% and higher, the RMSE is 0.010% and 95% of the observed errors for slopes of 0.1% or higher are within $\pm$ 0.016% (5th and 95th percentiles). For aspect, the magnitude of errors was inversely proportional to the magnitude of the slopes (abscissa; Figure S4). For slopes of 0.2% and higher, the RMSE is 2.9 degrees or lower, and 95% of the observed errors are within ± 4.8 degrees (5th and 95th percentiles). These results show that the errors in calculated slopes and aspects were relatively small compared to the observed range in the dataset. Hence, it is unlikely that correlations between pattern metrics and slope gradients, as observed in the main text, are strongly affected by the errors originating from the underlying topographical database.

Moreover, it should be noted that the above procedure may even be overestimating the errors associated with the AW3D30 dataset (from here referred to as the $30m$ elevation dataset). To generate the simulated errors, we used the global average standard deviation of the difference between the original AW3D $5m$ elevation dataset (from here referred to as the $5m$ dataset), from which the $30m$ dataset has been derived, and a reference LiDAR dataset. This standard deviation is $1.73m$ for gently sloping terrain (below 17.6%) (25). However, as the $30m$ elevation dataset was produced by averaging non-overlapping windows of 7 by 7 pixels of the $5m$ elevation dataset, the resulting standard deviation will be lower (26). Additionally, the ground slope in our study areas is at the lower end of the 0-17.6% range, namely below 1.5%, and therefore likely to suffer from smaller errors than reported for the whole range. Finally, the Somalian area we are studying displays relatively small errors in elevation measurements compared to other areas of the world (25).

E. Assessment of uncertainty in estimation of pattern frequency from optical imagery. The estimation of the dominant pattern frequency using a Fourier windowing technique introduces an unknown uncertainty in these estimations. This uncertainty stems from the decomposition of the signal into a discrete set of frequencies and from the noise in the analyzed (non-stationary) signal. To asses the model's uncertainty in the wavenumber estimations, we have used a simulation method. Specifically, we simulated 200 synthetic images, representing a two-dimensional sinusoid of each frequency class between 0.4 and 2.4 cycles $100m^{-1}$, with step size of 0.2. The directions of the sinusoidal waves were selected randomly and the signal was standardized to have zero mean and standard deviation of one. To mimic real images of vegetation patterns, we have added red noise with zero mean and standard deviation of 0.5 to each simulated signal. Red noise is a self-similar, or fractal, random spatial structure; this is a desirable property here because these are common in nature and especially in natural landscapes (27). The noise was created using the Fourier syn-

thesis technique with an energy spectrum exponent of 0.5 ([28]). Finally, in order to account for the fact that reflectance values are constant over the width of both vegetated and bare bands, the signal was converted to binomial values; that is, values between 0 and 1 were rounded to the nearest integer value. Several examples of simulated bands are presented in Figure S6.

Using the characteristics of the optical image windows of the Haud site (cell-size of $2.36m$ and windows 317 by 317 cells), the root-mean-square error of the estimated frequency was 0.082 cycles $100m^{-1}$. For the Sool (cell-size of $2.36m$ and windows 425 by 425 cells), the root-mean-square error was 0.044 cycles $100m^{-1}$. The magnitude of this error is significantly less than the observed variability in frequency in both sites (for every slope bin of Figure 3 in the main text, Levene's test, $P < 0.001$), showing significance of the observed wavenumber spread in both study sites.

1. Siteur K, et al. (2014) Beyond Turing: The response of patterned ecosystems to environmental change. *Ecological Complexity* 20:81–96.
2. Klausmeier CA (1999) Regular and irregular patterns in semiarid vegetation. *Science* 284(5421):1826–1828.
3. Funk C, et al. (2015) The climate hazards infrared precipitation with stations—a new environmental record for monitoring extremes. *Scientific data* 2:150066.
4. Deblauwe V, et al. (2016) Remotely sensed temperature and precipitation data improve species distribution modelling in the tropics. *Global Ecology and Biogeography* 25(4):443–454.
5. Hemming CF (1965) Vegetation arcs in Somaliland. *Journal of Ecology* 53(1):57–67.
6. Lauenroth WK, Adler PB (2008) Demography of perennial grassland plants: survival, life expectancy and life span. *Journal of Ecology* 96(5):1023–1032.
7. Canfield R (1957) Reproduction and life span of some perennial grasses of southern Arizona. *Rangeland Ecology & Management/Journal of Range Management Archives* 10(5):199–203.
8. Wright RG, Van Dyne GM (1976) Environmental factors influencing semidesert grassland perennial grass demography. *The Southwestern Naturalist* pp. 259–273.
9. Deblauwe V, Couteron P, Bogaert J, Barbier N (2012) Determinants and dynamics of banded vegetation pattern migration in arid climates. *Ecological Monographs* 82(1):3–21.
10. Gowda K, Iams S, Silber M (2018) Signatures of human impact on self-organized vegetation in the Horn of Africa. *Scientific Reports* 8(1):3622.
11. Schmidt J, Evans IS, Brinkmann J (2003) Comparison of polynomial models for land surface curvature calculation. *International Journal of Geographical Information Science* 17(8):797–814.
12. Bouvet A, et al. (2018) An above-ground biomass map of African savannahs and woodlands at 25 m resolution derived from ALOS PALSAR. *Remote Sensing of Environment* 206:156–173.
13. Mermoz S, Le Toan T, Villard L, Réjou-Méchain M, Seifert-Granzin J (2014) Biomass assessment in the Cameroon savanna using ALOS PALSAR data. *Remote sensing of environment* 155:109–119.
14. Bruniquel J, Lopes A (1997) Multi-variate optimal speckle reduction in SAR imagery. *International journal of remote sensing* 18(3):603–627.
15. Grodecki J, Dial G (2003) Block adjustment of high-resolution satellite images described by rational polynomials. *Photogrammetric Engineering & Remote Sensing* 69(1):59–68.
16. Couteron P, Lejeune O (2001) Periodic spotted patterns in semi-arid vegetation explained by a propagation-inhibition model. *Journal of Ecology* 89(4):616–628.
17. Couteron P (2001) Using spectral analysis to confront distributions of individual species with an overall periodic pattern in semi-arid vegetation. *Plant Ecology* 156(2):229–243.
18. Barbier N, Couteron P, Lejoly J, Deblauwe V, Lejeune O (2006) Self-organized vegetation patterning as a fingerprint of climate and human impact on semi-arid ecosystems. *Journal of Ecology* 94(3):537–547.
19. Deblauwe V, Couteron P, Lejeune O, Bogaert J, Barbier N (2011) Environmental modulation of self-organized periodic vegetation patterns in Sudan. *Ecography* 34(6):990–1001.
20. Penny GG, Daniels KE, Thompson SE (2013) Local properties of patterned vegetation: quantifying endogenous and exogenous effects. *Phil. Trans. R. Soc. A* 371(2004):20120359.
21. Renshaw E, Ford E (1984) The description of spatial pattern using two-dimensional spectral analysis. *Vegetatio* 56(2):75–85.
22. Otsu N (1979) A threshold selection method from gray-level histograms. *IEEE transactions on systems, man, and cybernetics* 9(1):62–66.
23. Barbier N, Couteron P, Planchon O, Diouf A (2010) Multiscale comparison of spatial patterns using two-dimensional cross-spectral analysis: application to a semi-arid (gapped) landscape. *Landscape ecology* 25(6):889–902.
24. Purinton B, Bookhagen B (2017) Validation of digital elevation models (DEMs) and comparison of geomorphic metrics on the southern Central Andean Plateau. *Earth Surface Dynamics* 5(2):211.
25. Takaku J, Tadono T, Tsutsui K, Ichikawa M (2016) Validation of 'AW3D' global DSM generated from ALOS prism. *ISPRS Annals of Photogrammetry, Remote Sensing & Spatial Information Sciences* 3(4).
26. Tadono T, et al. (2016) Generation of the 30 m-Mesh global digital surface model by ALOS PRISM. *International Archives of the Photogrammetry, Remote Sensing & Spatial Information Sciences* 41.
27. Keitt TH (2000) Spectral representation of neutral landscapes. *Landscape Ecology* 15(5):479–494.
28. Deblauwe V, Kennel P, Couteron P (2012) Testing pairwise association between spatially autocorrelated variables: A new approach using surrogate lattice data. *PloS one* 7(11):e48766.
29. Deblauwe V, Barbier N, Couteron P, Lejeune O, Bogaert J (2008) The global biogeography of semi-arid periodic vegetation patterns. *Global Ecology and Biogeography* 17(6):715–723.
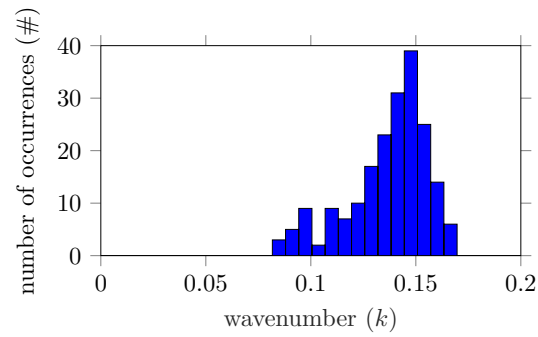
Fig. S1. Histogram demonstrating a spread in wavenumber (k) at the end of 200 simulations of the extended-Klausmeier model on a flat terrain ($v = 0$) with model parameters $e = 500$ and $m = 0.45$. These simulations had a random initial configuration close to a stable fully vegetated state. A climate change was simulated by decreasing the rainfall parameter a linearly from 3 to 0.5 over the course of 10^5 time unit, causing several pattern selections and corresponding changes in wavenumber.
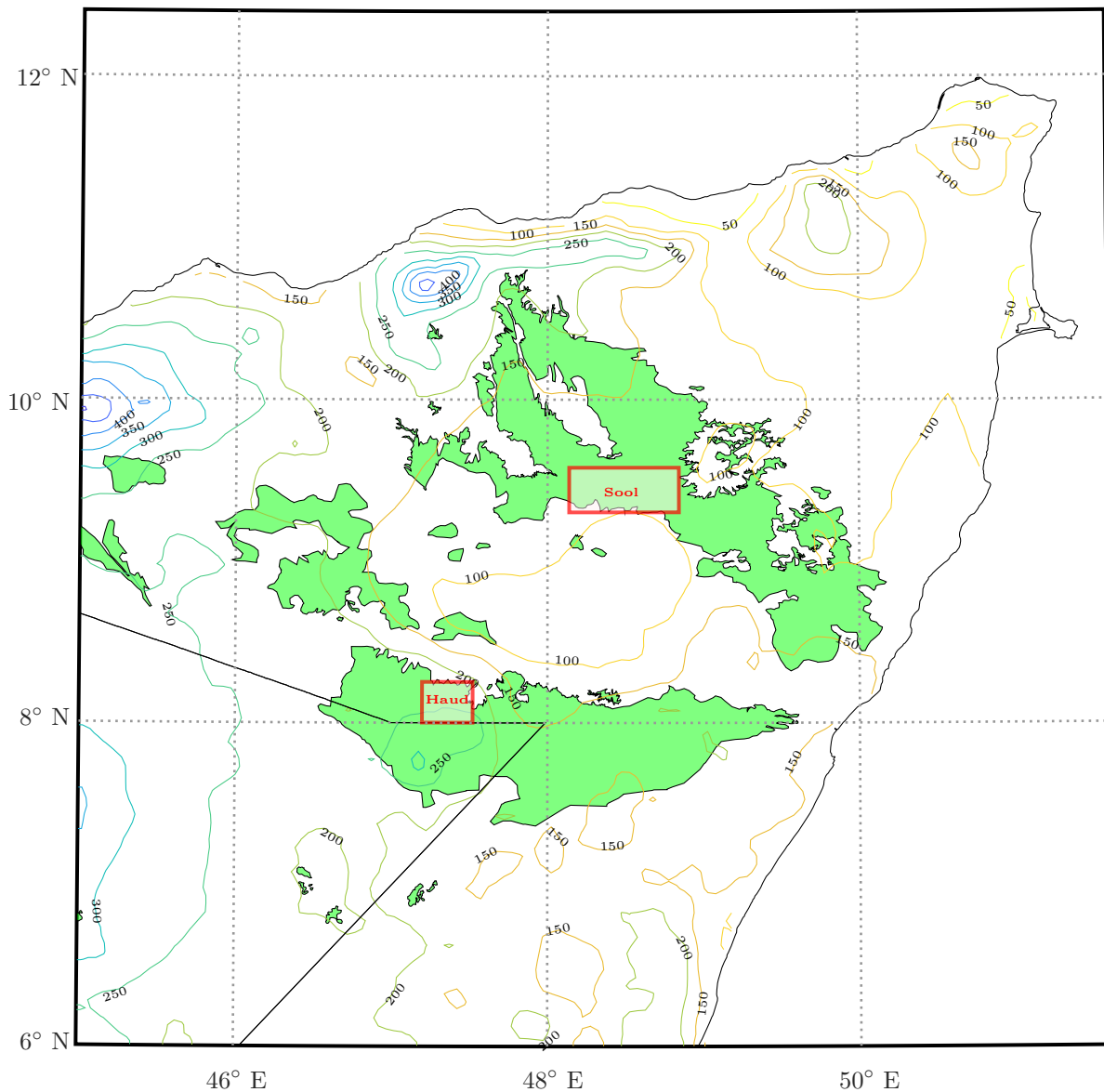
Fig. S2. Locations of the study sites and rainfall gradient in the Horn of Africa. The 'Haud' site ($8°0'14''$ to $8°15'11''$N; $47°11'54''$ to $47°31'4''$E) has a mean annual rainfall of 210–$270 mm\ yr^{-1}$ whilst the 'Sool' site ($9°18'49''$ to $9°34'34''$N; $48°8'15''$ to $48°43'15''$E) has a mean annual rainfall of 100–$140 mm\ yr^{-1}$. The distribution of periodic vegetation pattern shown in green is adapted from (29). Precipitation data was extracted from Climate Hazards Group InfraRed Precipitation with Stations (3) and is averaged over the years 1981–2013.
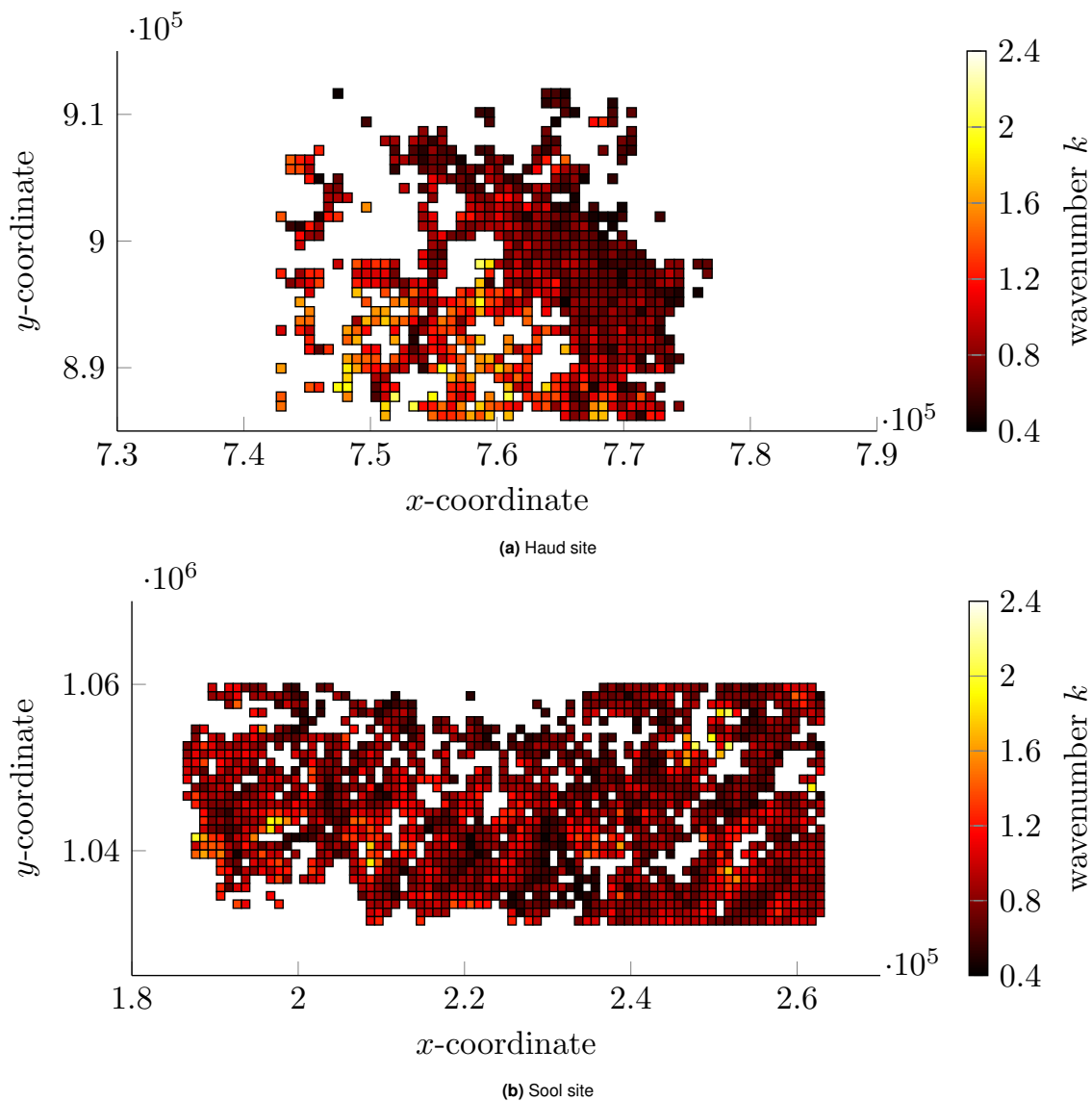
(a) Haud site

(b) Sool site

Fig. S3. The distribution of the measured banded pattern's wavenumber over the Haud site (a) and the Sool site (b). Here, darker red indicates a lower wavenumber and lighter yellow a higher wavenumber. On the x- and y-axes the UTM coordinates of the locations are given.
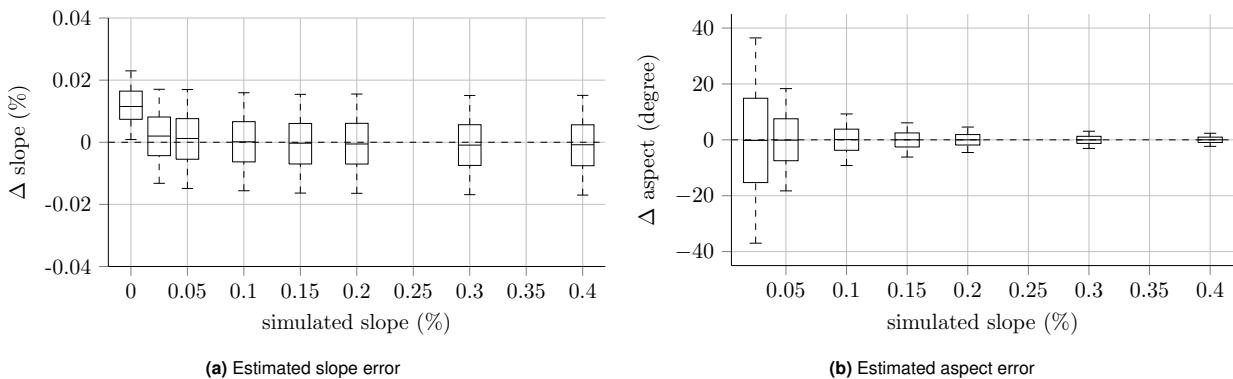

(a) Estimated slope error

(b) Estimated aspect error

Fig. S4. Slope (a) and aspect (b) estimation error from simulated topographical surfaces. Median errors are shown as horizontal bars with 25th–75th percentile ranges (boxes) and 5th and 95th percentile outlier cutoffs (whiskers). Note that aspect error could range from -180 to $+180$ degrees but has been cropped to largest measured error for visual purpose.
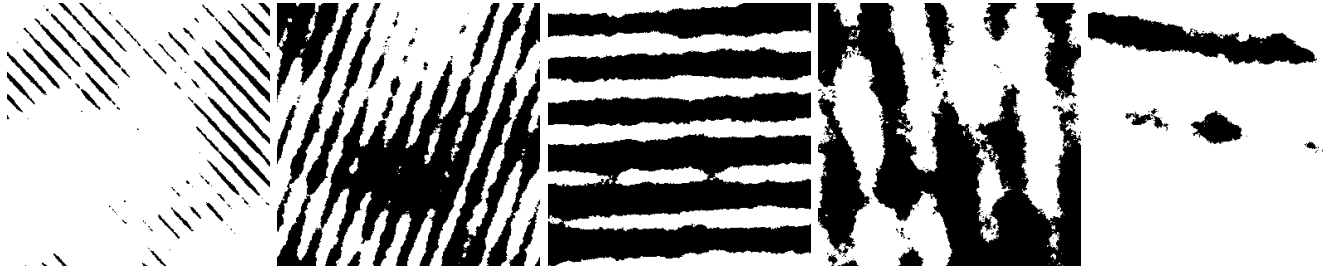
Bastiaansen et al.

Fig. S5. Examples of simulated vegetation patterns with frequency decreasing from left (2.4 cycles $100m^{-1}$) to right (0.4 cycles $100m^{-1}$).
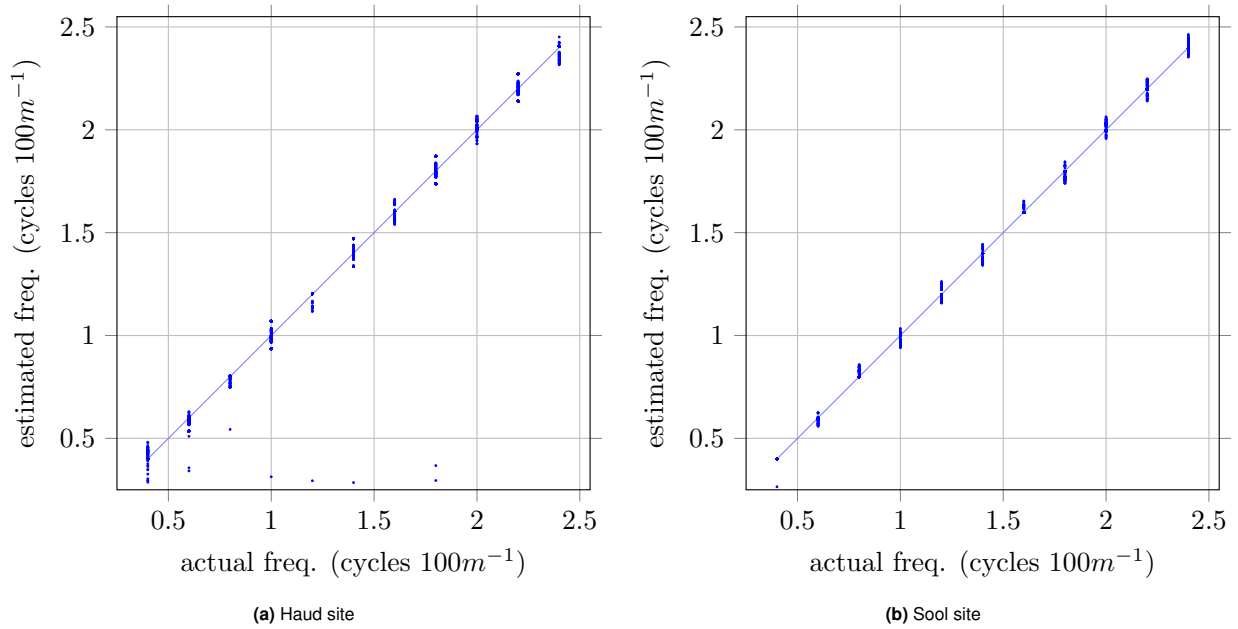

(a) Haud site

(b) Sool site

Fig. S6. Pattern frequency estimation error for the Haud (a) and the Sool (b) sites. Actual frequency of the simulated patterns and the corresponding estimation of these frequencies is shown by the blue dots. The straight line represents the perfect estimation line.